

Revealing the Two ‘Horns’ of Taurus with *Gaia* DR2

GRAHAM D. FLEMING,¹ JASON M. KIRK,¹ DEREK WARD-THOMPSON,¹ AND KATE M. PATTLE^{2,3}

¹*Jeremiah Horrocks Institute, University of Central Lancashire, Preston, PR1 2HE, UK*

²*Institute for Astronomy and Department of Physics, National Tsing Hua University, No. 101, Section 2, Guangfu Road, Hsinchu 30013, Taiwan*

³*Centre for Astronomy, School of Physics, National University of Ireland Galway, University Road, Galway, Ireland*

Submitted to ApJ

ABSTRACT

We investigate the spatial properties of sources from the *Gaia* catalogue previously identified as being members of the Taurus star forming region and which appear in the *Spitzer* catalogue. We study an area of sky of $10^\circ \times 15^\circ$, centred on Right Ascension (2000.0)=68.5° and Declination (2000.0)=27.0°, this being an area surrounding the Taurus molecular cloud. We use data obtained from the *Gaia* DR2 release. By using an inversion of *Gaia* parallax measurements to obtain distance values and by defining limits to the proper motions of the Taurus moving group, we are able to show that there are substantial differences in depth within the Taurus complex. Our results suggest that the Taurus cloud has significant depth and that there are two main associations centred at $\sim 130 \pm 6$ pc and $\sim 160 \pm 4$ pc at 1σ . These two associations also have different proper motions, of 24.5 ± 2.8 and 20.1 ± 2.4 mas yr⁻¹ respectively. We here label them the ‘Two Horns’ of Taurus.

Keywords: ISM: individual objects (Taurus molecular cloud) - stars: distances - parallaxes - proper motions

1. INTRODUCTION

The Taurus molecular cloud (TMC) is one of the closest low-mass star-forming regions, lying at a commonly accepted distance of roughly 140 pc (Elias 1978). The region covers some 10 to 15 degrees in extent which equates to about 25 to 30 pc at this distance. This makes comprehensive studies of the entire stellar population of the region difficult and few comprehensive studies of the three-dimensional structure of the cloud complex have previously been conducted (e.g. Luhman 2018). Situated within the TMC are numerous filaments and smaller cloud structures (Hartmann 2002; Schmalzl et al. 2010; Kirk et al. 2013; Panopoulou et al. 2014; Marsh et al. 2016). Previous studies have shown that young stars are grouped in and around these smaller structures (Gomez et al. 1993; Kirk et al. 2013). Early distance measurements (McCuskey 1939) determined a distance of 142 pc to the Taurus star-forming region, whilst later studies (Straizys & Meistas 1980; Meistas & Straizys 1981) of a number of Lynds dark clouds in the region (Lynds 1962) indicated that the TMC is more extended and exists between about 140 and 175 pc.

A study by Bertout et al. (1999) of three distinct regions of the complex placed the Lynds cloud L1495 at 125.6^{+21}_{-16} pc, the Auriga region at 140^{+16}_{-13} pc, and the southern region at 168^{+42}_{-28} pc.

The investigation of early-type O and A stars located in the Taurus-Auriga molecular cloud (Mooley et al. 2013) within 1σ parallax error of $6.2 < \pi < 7.8$ milli-arcsec (128 to 162 pc), identified a significant number of previously unidentified A5 or earlier stars within the region. Mooley et al. (2013) also noted in their study that even their new

distribution fell far short of the expected number of such stars if a standard log-normal IMF distribution is assumed for the region, adding to the discussion previously noted by Goodwin et al. (2004) and other researchers (e.g. Kraus et al. 2017).

In their study, Bertout & Genova (2006) derived kinematic parallaxes of 67 members of the Taurus moving group with typical errors of 20% and identified weak-line and classical T Tauri stars spread over distances between 106_{-24}^{+42} and 259_{-42}^{+61} pc. Very Long Baseline Array (VLBA) parallax observations of the Taurus star-forming regions conducted by Torres et al. (2007, 2009) showed a difference in the distances to separate regions of the Taurus complex by studying a small sample of individual sources. They noted a distance of 161.2 ± 0.9 pc for the star HP Tau/G2 and 146 ± 0.6 pc for T Tau (from Loinard et al. (2007)) in the eastern part of the complex, and 130 pc to the central area of the star-forming complex, by observing the T Tau-type stars Hubble 4 (V* V1023 Tau) at 132 ± 0.5 pc and HDE 283572 at 128.5 ± 0.6 pc. A multi-wavelength photometric study of the Taurus region Gudel et al. (2007) using *Spitzer* and *XMM-Newton* data produced large-scale maps detailing the stellar and substellar distribution of the region, and in a similar survey of the TMC conducted by Rebull et al. (2010), pre-main sequence members of the Taurus molecular clouds were identified using the *Spitzer* Space Telescope Taurus project (SSTtau) catalogue (<http://cds.u-strasbg.fr/cgi-bin/Dic-Simbad?SSTtau>) and Two-Micron All-Sky Survey (2MASS) data (<http://vizier.u-strasbg.fr/cgi-bin/VizieR?-source=B/2mass>).

In other, more recent research, planetary-mass brown dwarfs in the Taurus and Perseus star-forming regions have been investigated using photometric and proper motion data from a number of space and ground-based platforms including *Spitzer* and *Gaia* DR1 (Esplin & Luhman 2017).

Galli et al. (2018) presents trigonometric parallax and proper motion observations of Young Stellar Objects (YSOs) in the Taurus region as part of the Gould Belt Distances Survey using the VLBA. Their data suggest a significant difference between the closest and farthest stars in their sample of about 36 pc with the closest lying at 126.6 ± 1.7 and the most distant at 162.7 ± 0.8 pc. Within this range they noted that the central portion of the L1495 dark cloud is at 129.5 ± 0.3 pc, whilst the supposedly associated B216 structure lies at 158.1 ± 1.2 pc. The more recent comparison of *Gaia* DR2 and VLBI astrometry results (Galli et al. 2019) revise these distances but again confirm the existence of significant depth effects within the TMC.

Contemporary studies of the TMC using *Gaia* DR2 data conducted by (Luhman 2018; Esplin & Luhman 2019), present comprehensive studies of the stellar membership of the Taurus region. In both studies extensive reference is made to earlier works with regard to the stellar membership of specific cloud complexes within the TMC and the kinematics of their members. No evidence for an older population of stars previously identified by Kraus et al. (2017) and Zhang et al. (2018) is found, however the existence of a possible moving group of stars at a distance of 116 to 127 pc with ages of ~ 40 Myr first identified in the *Gaia* DR1 data by Oh et al. (2017) is suggested.

Previous studies such as those listed above have identified significant distance dispersion among the stellar members of various regions within the TMC star-forming complex, and have further suggested considerable depth effects within the cloud. In contrast to more recent studies, we revisit the coherent catalogue of sources identified by Rebull et al. (2010) in the *Spitzer* SSTtau catalogue and use the newly available data from *Gaia* data release 2 to model the characteristics and detailed internal distribution of sources within the region as a whole (Brown et al. 2018; Luhman 2018). Where our studies overlap, we note that our findings are consistent with those of Luhman (2018) and Galli et al. (2019) and consider them complementary to the results of these studies.

Section 2 provides a brief overview of the *Gaia* mission and some of the relevant issues concerning DR2. The acquisition of data and its subsequent analysis are discussed in §3 with particular attention being paid to the statistical treatment of the data. Section 4 presents a discussion of our data which is briefly summarised in §5. A compendium of the sources discussed in this study are presented in the Appendix.

2. GAIA

The European Space Agency *Gaia* astrometric space observatory (Lindegren & Perryman 1996) was launched in December 2013. The spacecraft is designed to measure the parallax, positions and proper motions of stars, with the ambitious goal of producing a three-dimensional map of most of our Galaxy. *Gaia* is not designed to measure distances directly, but they can be inferred through the determination of stellar parallax. The *Gaia* Archive¹ is a relational database which can be accessed through an interactive user interface and interrogated using conditional queries.

¹ <http://gea.esac.esa.int/archive/>

The second *Gaia* data release (DR2) occurred in April 2018 with a five-parameter astrometric solution for more than 1.33×10^9 sources (Brown et al. 2018). DR2 parallax uncertainties are in the range of up to 0.04 milli-arcseconds (mas) for sources with a broad-band, white-light magnitude (G) < 15 and in the order of 0.7 mas at $G=20$. Coupled with proper motion measurements from DR2, a detailed investigation of the internal kinematics of the Taurus star-forming region can be made. Due to the relative proximity of the Taurus star-forming region, where the parallaxes are positive and relative uncertainties are small, a Bayesian prior is not employed in this study (Bailer-Jones 2015; Bailer-Jones et al. 2018; Luri et al. 2018), and a straightforward inversion of parallax is used to infer distance. This does not affect any of the conclusions in this paper.

Since it is known that there are unquantifiable (but probably small) parallax errors due to a poorly determined zero-point offset in extinction (Lindegren et al. 2018), it is not possible to correct individual *Gaia* parallax values completely. It should also be remembered that *Gaia* is, in essence, an optical telescope and, as such, will have difficulty in accurately measuring parallaxes in areas of high optical extinction due to dust. Hence, for the purposes of this study, mean parameter values are used. Independent comparisons of *Gaia* and VLBA studies of YSOs in the Ophiuchus, Serpens and Aquila regions (Ortiz-León et al. 2018) obtained consistent parallax values across all systems, supporting our use of uncorrected *Gaia* parallax values at this distance.

3. DATA

3.1. Selection and discussion

Sources towards the Taurus region were selected using a $15^\circ \times 10^\circ$ box centred on RA (2000.0)= 68.5° and Dec (2000.0)= $+27.0^\circ$. This effectively defines an area on the sky of roughly 126 pc^2 at the approximate distance of the Taurus cloud. Parallax values were set between 5.0 and 10.0 mas, setting a box covering a distance range from 100 to 200 pc. Quality limits were set to only include data with at least 5 independent astrometric measurements. No other quality flags were defined, so as to maximise the number of sources returned, thereby enabling an objective selection of sources within the study area. After performing distance calculations on the mean parallax values of the sources returned, the results were plotted on a histogram in 1 pc bins. The subsequent distribution showed no evidence of the expected peak in population at around 140 pc. We hypothesised that this was due to the Taurus sources being totally swamped by foreground and background objects. To remove possible contamination of our sample by foreground and background field stars, we cross-referenced our findings with the *Spitzer* SSTtau catalogue (Rebull et al. 2010) and obtained 168 objects in our search area with known *Gaia* parallaxes and proper motions.

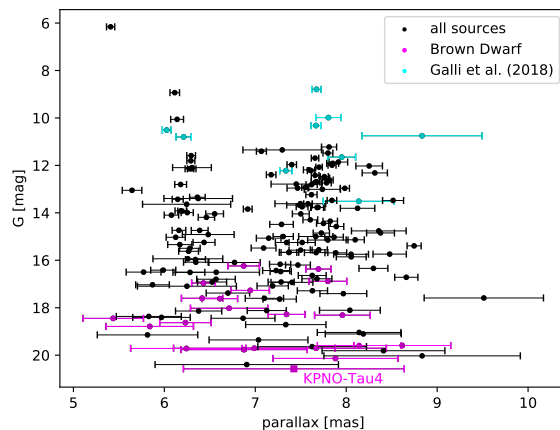


Figure 1. Parallaxes, with errors, of the 168 *Gaia* DR2 sources identified in the *Spitzer* SSTtau catalogue of Taurus members, plotted against G-Band mean magnitude. Sources identified in the SIMBAD Astronomical Database as brown dwarfs are shown in magenta whilst those cross-matched to Galli et al. (2018) are in cyan.

Within this subset the largest parallax error is 1.214 mas for object *Gaia* DR2 151265002954775936 (KPNO-Tau4), which is a classified L0 brown dwarf (see Figure 1). It should be noted, that brown dwarfs within the sample typically have higher parallax errors, suggesting constraints on the detection of such low luminosity objects. Parallax errors on the remaining sources are significantly lower. Parallax errors in relation to *Gaia* DR2 G-band magnitude

(*phot_g_mean_mag*) for the sources identified in the *Spitzer* catalogue are presented in Figure 1 which clearly shows a double peaked scattering in the parallax (and hence, distance) distribution of the sources. Figure 1 also provides a comparison to those of our sources which are present in the Galli et al. (2018) study and it can be seen that these sources are amongst the brightest of those in our study.

The properties of the 168 *Gaia* sources are listed in Table 3 in Appendix A. Taking inverse parallax values and determining the distances of our sample of 168 sources, we binned the values at 3 pc intervals and produced a distance distribution. The resulting distribution is plotted in Figure 2. The same double-peaked distribution seen in Figure 1 is visible.

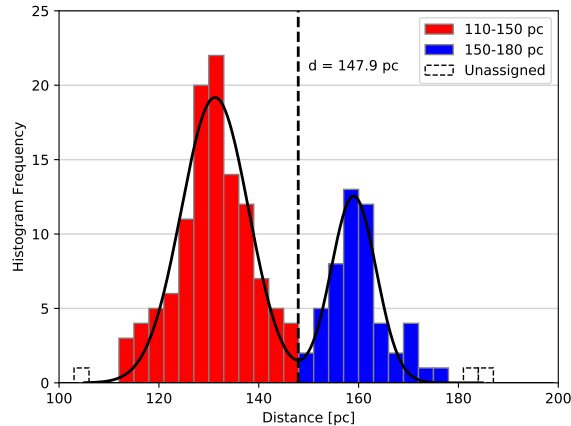


Figure 2. Distance distribution of 168 *Gaia* DR2 sources identified in the *Spitzer* SSTtau catalogue of Taurus members. Sources are grouped in 3-pc bins. Two distinct groupings are seen. A double-Gaussian curve is fitted identifying a minimum value at 147.9 pc (see text for details).

A double-Gaussian curve (shown in black) is fitted (Figure 2) indicating a minimum in the bi-modal distribution at 147.9 pc, hereafter taken to be ~ 150 pc.

3.2. Validation of *Gaia* DR2 distance data

We have compared the *Gaia* DR2 distance data with previous VLBA determinations (Torres et al. 2009; Galli et al. 2018) to draw comparisons between the two sets of observations and find nine sources common to both studies. These sources are amongst the brightest of our sources and are identified in Figure 1, showing their *Gaia* G-Band mean magnitudes.

Figure 3 plots the two sets of distances of these common sources. It can be seen that the *Gaia* DR2 derived values are roughly consistent with previous measurements. There are three sources which show large errors, *Gaia* DR2 147778490237623808 (V807 Tau B), *Gaia* DR2 148116246425275520 (V999 Tau) and *Gaia* DR2 163233981593016064 (V1096 Tau). SIMBAD identifies V999 Tau and V1096 Tau as being M0.6 class T-Tauri stars whilst V807 Tau B is listed as a K7 T-Tauri star. *Gaia* DR2 G-band extinction data for V1096 Tau is recorded as being 2.97 mag but is incomplete for the other two sources, it is therefore not possible to make a definitive judgement concerning the large errors displayed by these objects. However, agreement for the other sources is clearly seen.

3.3. Statistical analysis of distance distribution

To analyse the distribution of our sources we used Hartigans’ dip test for uni-modality (Hartigan et al. 1985; Maurus & Plant 2016). This is recognised as being a robust statistical measure of the modality of a continuous distribution where the ‘dip’ measures the departure of a distribution from uni-modality. The Hartigan Dip Statistic (HDS), corresponding to the probability ‘p-value’, is determined by repeatedly sampling the maximum difference between the observed distribution of data and that of a uniform distribution that is chosen to minimize this maximum difference. P-values < 0.05 are an indication of significant bi-modality and values greater than 0.05 but less than 0.10 suggest bi-modality with marginal significance. We obtained a p-value of 0.025. This value suggests that we reject the null hypothesis of uni-modality. We therefore identify our distribution as bi-modal with a boundary between the two groups at ~ 150 pc.

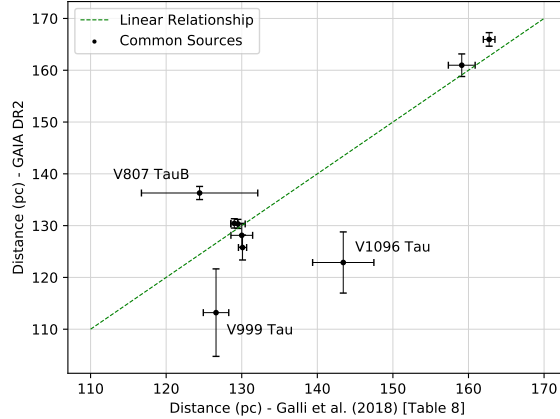


Figure 3. Comparison of *Gaia* DR2 and VLBI (Galli et al. 2018) distance data for the nine common sources.

Having statistically identified that our distance distribution represents two independent populations we split them into ‘near’ and ‘far’ groups using the ~ 150 pc boundary to give groups lying between 110 to 150 pc and 150 to 180 pc respectively. Figure 2 identifies our two groups, colour coded red and blue for the ‘near’ and ‘far’ groups respectively. The three sources coded white lie outside the two main populations and are not discussed hereafter. We here identify our two main groups as the ‘Two Horns’ of Taurus. Our analysis is consistent with other recent *Gaia* studies of Taurus (Luhman 2018; Esplin & Luhman 2019).

3.4. Proper Motion studies

A number of proper motion studies have previously been undertaken of this region, notably those conducted by Jones & Herbig (1979); Walter et al. (1987); Hartmann et al. (1991); Gomez et al. (1992); Frink et al. (1997); Ducourant et al. (2005); Bertout & Genova (2006) and more recently (Dzib et al. 2015) and Galli et al. (2018). In general, these are all studies of pre-main sequence stars, seeking to identify the proper motions, μ , of members of the Taurus group. Table 1 lists the mean, upper and lower proper motion values from these studies. We have used these to constrain the upper and lower limits of proper motion for this study of the TMC.

All 168 identified sources (see Appendix A, Table 3) have *Gaia* DR2 proper motions, and of these, 165 lie within the ‘near’ and ‘far’ populations mentioned above – the remaining 3 are shown in white in Figure 2. Based on the literature values given in Table 1, for the purposes of this study, upper and lower limits of proper motion for the Taurus moving group are taken as being 40 mas yr^{-1} and 12 mas yr^{-1} respectively. Within these limits there are 161 sources. The four sources which lie outside of our limits have μ values of 5.41, 9.05, 43.38 and $45.40 \text{ mas yr}^{-1}$ which are consistent with the upper and lower ranges discussed in the literature, but in Appendix A, Table 3 we discounted these μ values since they are derived using extreme values of either RA or Dec. Discounting these four sources, our minimum, mean and maximum values of proper motion are given in Table 1.

Using a k-Means clustering algorithm we analysed this group to investigate whether there is a proper motion ‘split’ associated with the distance distribution and to determine the centroids of the groups if such an association exists. We find that such an association does exist and that the mean proper motions of the two groups are different. There are 111 members in the ‘near’ group and 50 in the ‘far’ group – the remaining 4 sources are rejected as lying outside of this $12\text{--}40 \text{ mas yr}^{-1}$ proper motion cut. The mean proper motion of the ‘near’ population is $24.5 \pm 2.8 \text{ mas yr}^{-1}$, and that of the ‘far’ population is $20.1 \pm 2.4 \text{ mas yr}^{-1}$.

The proper motions of 156 of the 161 stars are shown in Figure 4 (the colour coding of the two groups is the same as in Figure 2). Figure 4 has been ‘zoomed-in’ to show the bulk of the sources more clearly – so there are five sources lying within our proper motion limits of $12\text{--}40 \text{ mas yr}^{-1}$, but which are outside the plotted boundaries of Figure 4. Of these five, two belong to the ‘near’ population (Gaia DR2 146675954953119104 and Gaia DR2 147546080967742720), and three lie in the ‘far’ population (Gaia DR2 148116276529733120, Gaia DR2 147248216395196672 and Gaia DR2 145213192171159552). One of these sources, Gaia DR2 145213192171159552 (CoKu HP Tau G2) has been previously studied (Torres et al. 2009) using the VBLA, which determined a parallax of $6.2 \pm 0.3 \text{ mas}$. Our *Gaia* DR2 value is $6.02 \pm 0.04 \text{ mas}$ and is fully consistent.

Table 1. Taurus proper motion values in the literature.

Reference	μ_{min} (mas yr ⁻¹)	μ_{mean} (mas yr ⁻¹)	μ_{max} (mas yr ⁻¹)
Jones & Herbig (1979)	...	22.80	...
Frink et al. (1997)	...	21.24 ^a	...
Bertout & Genova (2006)	9.37	22.38	41.22
Slesnick et al. (2006) ^b	13.89	...	43.05
Torres et al. (2009) ^c	...	~ 20.0	...
Galli et al. (2018) ^d	15.0	~ 22.0	39.0
Mean literature values ^e	12.75	22.14	41.09
This study	11.94	23.02	30.60

^a Value given for the central part of the Taurus-Auriga cloud system.

^b Values derived from their figure 9 (lower histogram).

^c cited in Dzib et al. (2015).

^d Maximum and minimum values obtained from their figure 2.

^e Ignoring imprecise values from Torres et al. (2009) and Galli et al. (2018).

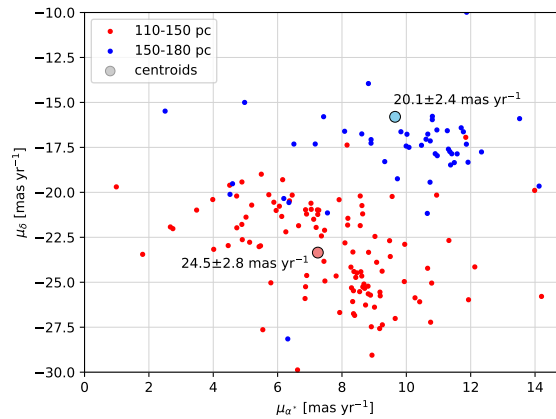


Figure 4. Proper motions for the ‘near’ and ‘far’ populations of 156 of the stars shown in Figure 2 with proper motion limits of 12 mas yr⁻¹ to 40 mas yr⁻¹. Colour coding is the same as in Figure 2. Two populations of proper motion groupings can be seen which are consistent with the two distance groupings seen in Figure 2. There are 2 red and 3 blue outlying sources beyond the area shown on this plot (see text for details).

For comparison, 7 sources from the study of Galli et al. (2018) lie within our ‘near’ population and 2 lie in the ‘far’ group. These numbers are statistically low, nevertheless they provide mean proper motions of 24.90 ± 4.88 and 19.66 ± 0.50 mas yr⁻¹ for the ‘near’ and ‘far’ populations respectively, which are fully consistent with the values found here.

4. DISCUSSION

It has been seen (Figure 2) that there are two significant peaks in the distance distribution, centred at approximately 130 and 160 pc. Separating these peaks into ‘near’ and ‘far’ populations, as indicated by the red and blue colouring in Figure 2, results in mean (and error on the mean) distances for each component of 130.6 ± 0.7 and 160.2 ± 0.9 pc respectively. For these groups the standard deviation on the distance is ~ 6 & ~ 4 pc respectively versus a mean error

on each measurement of ~ 4 -5 pc. It is probable that the standard deviations for the distances are broadened by these measurement errors. Table 2 shows the parameters of each group. These distributions are roughly consistent with the findings of previous studies mentioned in §1, but far more double-peaked than was previously realised.

Table 2. Properties of the near (red) and far (blue) populations shown in Figures 2 and 4.^a

	Number of Sources	Mean Distance [pc]	Standard Deviation [1 σ]	$\mu_\alpha \cos \delta$ [mas yr ⁻¹]	μ_δ [mas yr ⁻¹]	$ \mu_{Total} $ [mas yr ⁻¹]	Standard Deviation [1 σ]	Angle θ [degrees]	Standard Deviation [1 σ]
Near	111	130.6 \pm 0.7	6.7	7.5	-23.1	24.5	2.8	162	6
Far	50	160.2 \pm 0.9	4.5	8.9	-17.3	20.1	2.4	154	17

^a Statistics are calculated after distance and proper motion cuts have been made.

For the purposes of simplicity, we have identified our groups as lying at 110–150 pc and 150–180 pc respectively. From Figure 4 it can be seen that these two populations have markedly different proper motion characteristics. The populations fall within two separate and distinct proper motion groups, related to their distance. The mean proper motions of the two groups are listed in Table 1, and are 24.5 ± 2.8 and 20.1 ± 2.4 mas yr⁻¹ for the ‘near’ and ‘far’ populations respectively. The mean angles, θ , of the proper motions of the two populations are also listed in Table 2, along with their standard deviations. These are $162 \pm 6^\circ$ and $154 \pm 17^\circ$ for the ‘near’ and ‘far’ populations respectively, where all angles are measured east of north.

To confirm that our two groups are contained within the same distribution we examined our proper motion groups using a general-purpose non-parametric two-sample Kolmogorov-Smirnov (KS) test (Kolmogorov 1933). This two-sample test does not assume that data are taken from Gaussian distributions and is sensitive to differences in both location and shape of the two samples. This test is recognised by Peacock (1983) as being a powerful tool in the analysis of astronomical data. However, we recognise that caution needs to be taken when using this test in astronomical applications (e.g. Feigelson & Babu 2013; Stephens 1974).

The p-value provided by this test can be interpreted in the same way as p-values for other such tests. If the p-value is small, the null hypothesis that the two samples were drawn from the same distribution can be rejected and it can be assumed that the two groups were sampled from populations with different distributions. We obtain a p-value of 4×10^{-17} which supports our earlier identification of a non-unimodal distribution (see §3.3) and rejects the possibility that the two groups come from the same population.

4.1. Group and structure correlations

Using the data presented in Figures 2 and 4 it is now possible to obtain a picture of the distribution of objects within our sample region. Figure 5 presents this distribution superposed on a visual extinction map of the region calculated from the 2MASS survey (Schneider et al. 2011). Obvious structures within the distance distribution of sources are identifiable within the cloud complex. For example, Gaia DR2 164422961683000320 (V1070 Tau), which lies within the south-eastern region of Barnard’s Cloud B10 (part of the extended Lynds L1495 filament), is found to lie at 126.4 ± 1.6 pc, which is consistent with the value of 126^{+21}_{-16} pc found earlier by Bertout et al. (1999). The region around B10 can thus be seen to be part of the ‘near’ population, and the 31 sources associated with the ‘near’ group within B10 are found to have a mean distance of 131.9 ± 3.2 pc, with a standard deviation of 5.0 pc.

Stretching away to the south-east from B10 lies the L1495 filament and its associated clouds B211 and B213. There are a number of sources from both populations which lie directly within, or close to this structure. It is apparent that, if these sources are genuinely associated with the filament, then there appears to be a double distance gradient along this structure. One interpretation of this apparent double gradient is that the cluster of ‘far’ population sources roughly aligned with B213, are actually background to it. For this to be the case, there would need to be gaps in the foreground cloud that allowed the background region to be seen. This explanation would be consistent with the findings of Hacar et al. (2013), if one interprets their line-of-sight velocity with distance. This hypothesis is pursued

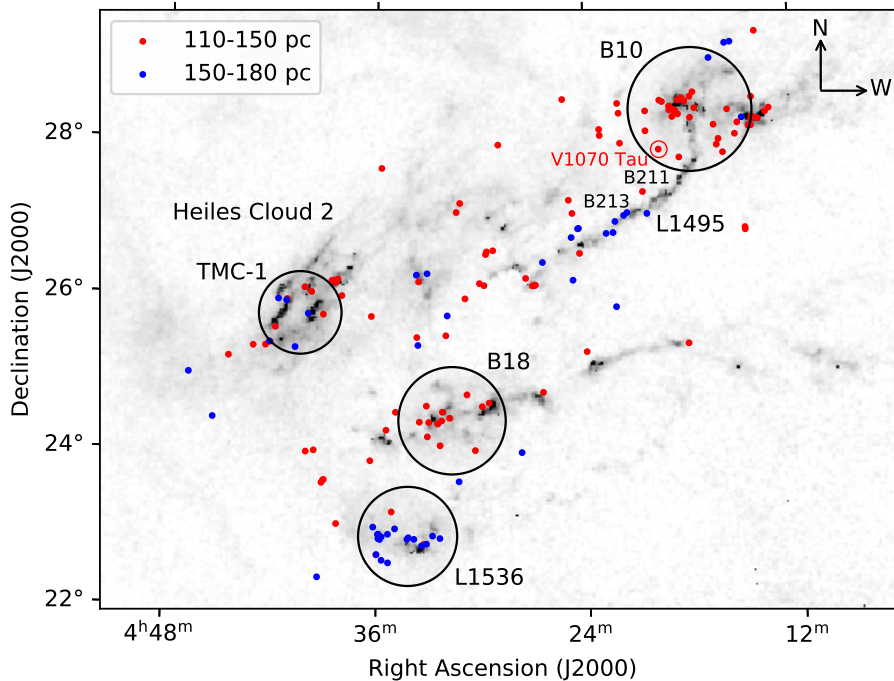


Figure 5. Spatial distribution of *Gaia* DR2 sources identified in the *Spitzer* SSTtau catalogue, using appropriate selection criteria (see text for details). Sources have been identified according to distance and overlaid on a visual extinction map calculated from the 2MASS survey (Schneider et al. 2011). The colour coding is the same as in Figures 2 and 4. It can be seen that both B10 and B18 are dominated by sources in the ‘near’ group. L1536 is predominantly composed of sources from the ‘far’ population. See text for further discussion.

further in §4.3.1 below. Cloud B18 appears to be populated with a discrete population belonging to the ‘near’ group. Analysis of the data for this group shows that they are lying at a mean distance of 127.4 ± 3.8 pc, with a standard deviation of 7.9 pc.

The VLBA derived parallax to the star HP Tau/G2 in L1536 provides a distance of 161.2 ± 0.9 pc (Torres et al. 2009). HP Tau/G2 also appears in the Galli et al. (2018) study with a derived mean distance of 162.7 ± 0.8 pc, which is within 3σ of the *Gaia* value of 165.9 ± 1.3 pc. This star is embedded within the reflection nebula GN 04.32.8, which appears as a crescent-shaped feature in the Herschel column density map of L1536 (Kirk et al. 2013). HP Tau/G2 (*Gaia* DR2 145213192171159552) lies within the area of L1536 (Figure 5). There are 20 ‘far’ group sources identified in this area with a mean distance of 160.3 ± 3.7 pc, and a standard deviation of 6.8 pc. The clear interaction of HP Tau/G2 with L1536 strongly implies that L1536 is at a comparable distance (Kirk et al. 2013). This is also supported by the earlier study of Bertout et al. (1999), which placed the southern region of the Taurus cloud at 168^{+42}_{-28} pc. There are seen to be two members of the near population situated within, or close to the L1536 region. These are *Gaia* DR2 145238687096970496 and *Gaia* DR2 145157937416226176 which have distance determinations of 130.0 ± 2.3 and 140.3 ± 4.2 pc respectively. When considering their maximum distances, they do not fall within the lower boundary of the ‘far’ group and we thus consider their proximity to L1536 as a fortuitous alignment and discount them as being members of L1536.

The association of our groups with the discrete structures within the Taurus cloud is graphically highlighted by Figure 5. With the addition of the *Gaia* DR2 derived distance data we are able to develop a three-dimensional picture of this region. So, we studied the 3-D spatial distribution of our sources in Galactic X, Y, and Z as well as celestial ICRS Right Ascension and Declination. Figure 6 presents our 165 sources in the Galactic reference frame ordered by Right Ascension. Of interest here are the lower panels which plot Galactic Z-Y and X-Y with the colour plots ordered by Right Ascension. The ‘near’ and ‘far’ group affiliations previously noted in the ICRS reference frame are clearly seen in Cartesian space with the spatial alignments, suggesting that the TMC is consistent with a structure similar to that of an inclined sheet facing away from us.

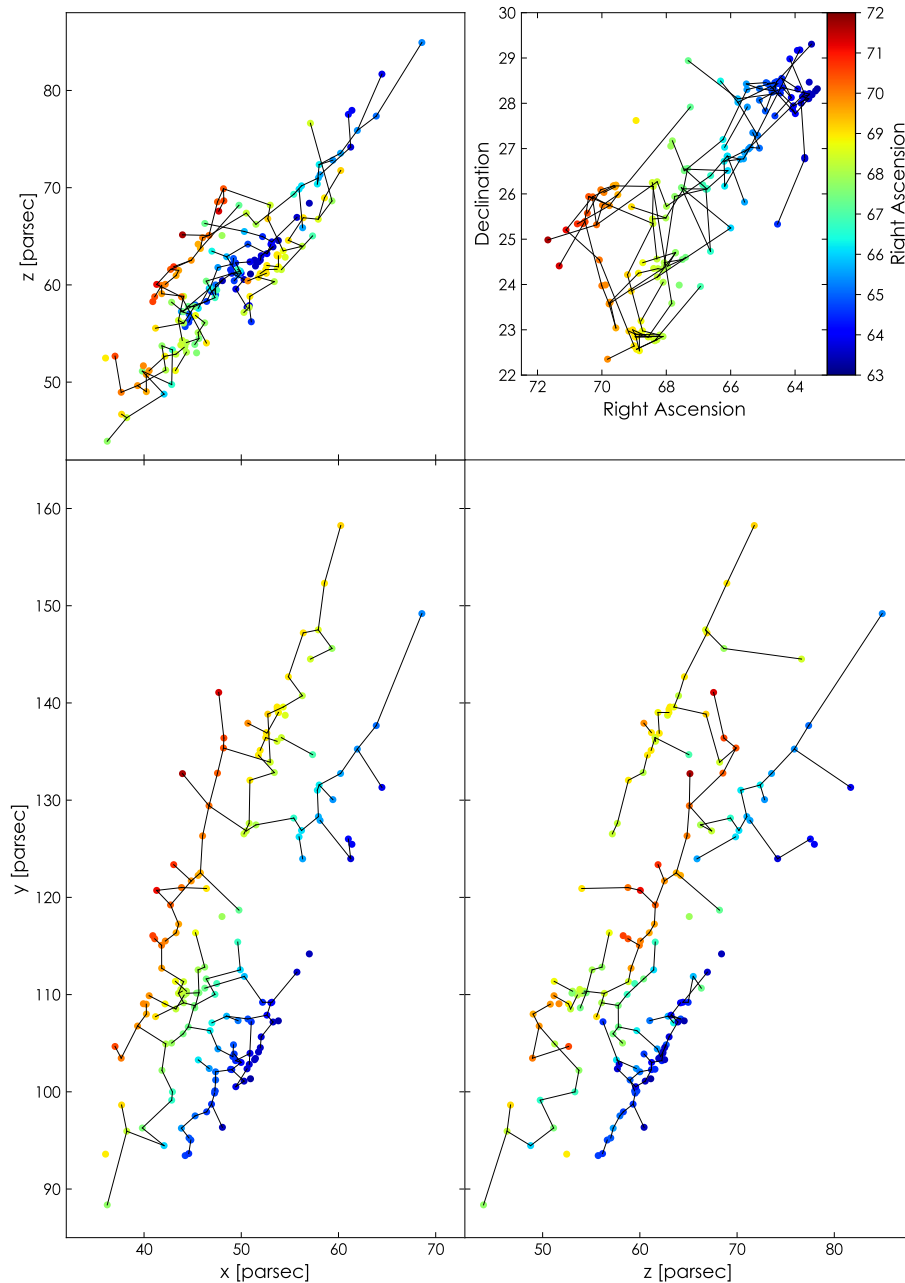


Figure 6. Distribution of 165 sources in the Galactic reference frame. The lower panels suggest that the stellar distribution resembles a ‘sheet like’ structure (see text).

4.2. TMC-1 and the Taurus Molecular ‘Ring’ (TMR)

Here, we consider the TMC-1 region in more detail. The area commonly known as the ‘Bull’s Tail’ (Nutter et al. 2008) lies within a region previously referred to as the Taurus Molecular ‘Ring’ (TMR), which is associated with the low mass star-forming Heiles Cloud 2 and has been the subject of many previous investigations (e.g. Hartigan & Kenyon 2003; Tóth et al. 2004; Nutter et al. 2008; Malinen et al. 2012). Previous studies of this feature provided a generic distance of ~ 140 pc in common with the region as a whole. However, Nutter et al. (2008) showed that this putative ‘ring’ is not a coherent structure, but rather a chance alignment of discrete sources with different line-of-sight velocities.

Objects Gaia DR2 148401565437820928 and Gaia DR2 148400229703257856 lie in the central region of the ‘Bull’s Tail’ and have *Gaia* DR2 derived distances of 136.3 ± 8.2 and 136.9 ± 2.1 pc respectively, which are in general agreement with previous studies. From Figure 5 it can be seen that there is a member of the ‘far’ group to the south of the ‘Bull’s Tail’ (Gaia DR2 148374391180009600). The association of members of both the ‘near’ and ‘far’ populations with this feature supports the previous suggestion of [Nutter et al. \(2008\)](#) that the TMR is not a coherent feature but is rather composed of disparate sources at different distances spread throughout the depth of the complex.

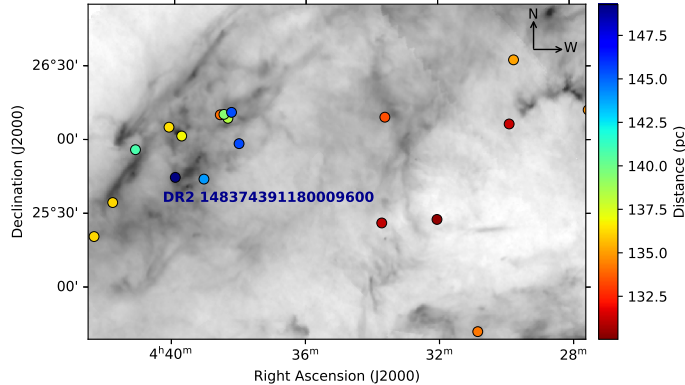


Figure 7. The region around TMC-1 with sources colour coded by distance. The putative ‘ring’ is situated to the east of the figure which clearly shows that the feature has significant depth.

Further, the region around the putative ‘ring’ is seen to the east of $4^h 36^m$ in Figure 7. It can clearly be seen that objects in this area have a spread in distance of some 10 to 15 pc. We are thus able to support the hypothesis of [Nutter et al. \(2008\)](#) that the so-called ‘ring’ is not a coherent structure.

4.3. Velocity distributions within the TMC

Here we look at the ‘true’ proper motions of our two populations by comparing literature values with our own findings.

4.3.1. Comparison between distance and line-of-sight velocity

We compare our interpretation of the three-dimensional nature of the TMC with existing line-of-sight velocity measurements of the region. It is well-established that the TMC has a complex velocity structure (e.g. [Clark et al. 1977](#)). In the context of the *Gaia* distance observations, it is a useful exercise to attempt to associate the stars in our ‘near’ and ‘far’ groups with the major line-of-sight velocity components of the cloud. The ^{12}CO emission associated with the TMC has systemic line-of-sight velocities ranging from $\sim 0 - 12 \text{ km s}^{-1}$, with the large majority of the emission having velocities in the range $4 - 8 \text{ km s}^{-1}$ ([Narayanan et al. 2008](#)). The TMC has an overall east-to-west velocity gradient, with the eastern parts of the cloud preferentially having a lower systemic velocity than those in the west (e.g. [Goldsmith et al. 2008](#)). However, there is a great deal of variation within this broad east-to-west trend. Particularly, the L1495 filament is known to have two distinct velocity components, separated by $\sim 1.5 \text{ km s}^{-1}$ (e.g. [Heiles & Katz 1976](#); [Clark et al. 1977](#)). [Hacar et al. \(2013\)](#) used C^{18}O observations to further separate these two components into multiple sub-filaments, with one set of sub-filaments having velocities $\sim 5 - 6 \text{ km s}^{-1}$, and the other having velocities $\sim 7 \text{ km s}^{-1}$. The well-defined plane-of-sky morphology of the L1495 filament is at odds with its apparent lack of velocity coherence, leading to suggestions that the ‘filament’ may in fact be an edge-on sheet (e.g. [Palmeirim et al. 2013](#)). However, [Li & Goldsmith \(2012\)](#) compared volume densities derived from dense gas tracers with 2MASS-derived column densities, and found that the high-density portion of the L1495 ‘filament’ has a plane-of-sky depth of only $\sim 0.12 \text{ pc}$, suggesting that it is indeed an approximately cylindrical structure.

The stars associated with the TMC included in the *Gaia* DR2 catalogue are located at intermediate visual extinction, and so are not associated with the densest star-forming gas. We thus compare the distribution of the stars in our two distance groups to the velocities measured in ^{12}CO observations of the TMC ([Narayanan et al. 2008](#); [Goldsmith et al. 2008](#)). These observations trace moderately dense gas ($n(\text{H}_2) \sim 10^2 - 10^3 \text{ cm}^{-3}$) which is definitively associated with the TMC, but which is not gravitationally unstable and actively forming stars (e.g. [di Francesco et al. 2007](#)).

^{12}CO velocity channel maps presented by [Narayanan et al. \(2008\)](#) show that the B10 and B18 regions have systemic velocities $\sim 7 \text{ km s}^{-1}$, while the L1536 region has a systemic velocity $\sim 5 \text{ km s}^{-1}$. The L1495 filament shows a double-peaked velocity structure, as discussed above. The TMC-1 region also has multiple velocities, with some suggestion that the eastern side of TMC-1 is at a lower systemic velocity ($\sim 5 - 6 \text{ km s}^{-1}$) than the western side (at $\sim 7 \text{ km s}^{-1}$).

We find a correspondence between these behaviours and the spatial distribution of the stars in our ‘near’ and ‘far’ groups (see Figure 5). B10 and B18 are both dominated by ‘near’ stars, and have a systemic velocity of $\sim 7 \text{ km s}^{-1}$, while L1536, containing ‘far’ stars, has a systemic velocity $\sim 5 \text{ km s}^{-1}$. The L1495 filament, with its two velocity components, contains stars from both groups, as does TMC-1. However, in TMC-1 the ‘far’ stars are preferentially located in the east, while the ‘near’ stars are preferentially located in the west, corresponding to a velocity gradient from $\sim 5 - 7 \text{ km s}^{-1}$ across the region. There is thus a qualitative tendency for ‘near’ stars to be associated with $\sim 5 \text{ km s}^{-1}$ sight-lines, and for ‘far’ stars to be associated with $\sim 7 \text{ km s}^{-1}$ sight-lines.

Our results thus tentatively suggest that the two main velocity components of the gas in the TMC are located at different line-of-sight distances, with the $\sim 5 \text{ km s}^{-1}$ gas being located in front of the $\sim 7 \text{ km s}^{-1}$ gas. The ‘gaps’ in the L1495 filament hypothesised in Section 4.1 are also seen in the velocity data.

4.3.2. Velocity directions

The Right Ascension and Declination proper motions of our sample sources are detailed in Table A. When these values are translated into vectors, as shown in Figure 8 (left), it can be seen that there is a small difference in the vectors between the two populations. The mean values of proper motion for each population and their standard deviations are given in Table 2. The arrows indicate the proper motions of the stars.

However, for a proper analysis of the relative proper motions the influence on these motions caused by the solar motion and Galactic rotation need to be taken into account. Literature studies suggest that this transform is particularly sensitive to the Oort constants ([Oort et al. 1927](#); [Olling & Dehnen 2003](#)), in particular the ‘V’ component of the solar motion relative to the Local Standard of Rest, which is unknown by up to a factor 2.

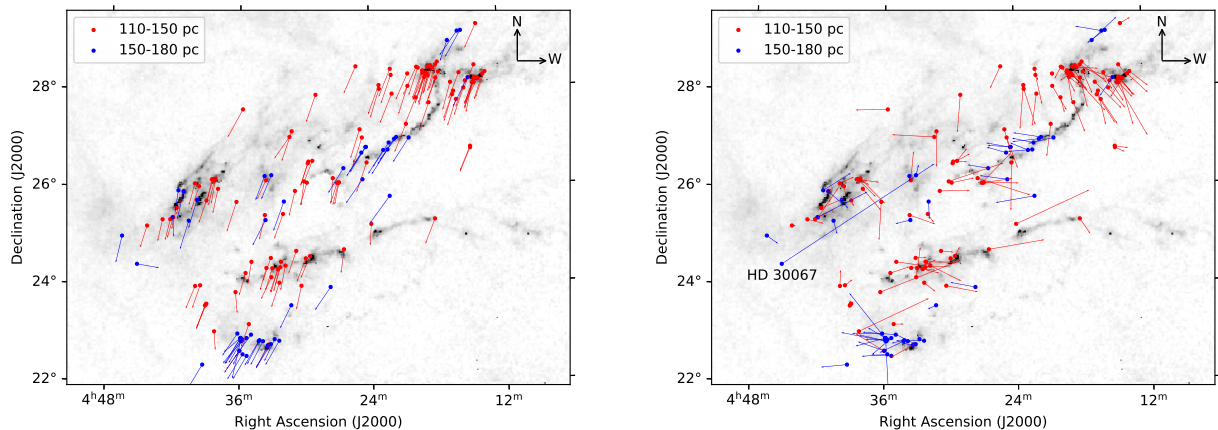


Figure 8. Group distributions within the TMC and related velocity vectors. Left: Proper motions of the ‘near’ and ‘far’ groups identified in Figure 2 (see text). Individual star proper motions displayed as vectors, showing direction and relative magnitude of velocity. Right: Proper motions after the removal of Solar and Galactic motion components towards Taurus.

We use the value of Oort constants from [Li & Goldsmith \(2012\)](#) and the Solar velocities from [Schönrich et al. \(2010\)](#) using the convention for solar velocities in the Galactic coordinate system as: U being the component toward the Galactic Center; V the component along the line of Galactic rotation; and W being the component out of the Plane, towards the Galactic North Pole.

Since it is also necessary to use a rotation matrix to transform between celestial ICRS (RA,Dec) and Galactic (l,b) coordinates we use the technique presented by [Li et al. \(2019\)](#). We also consider the treatment of barycentric stellar motion in astrometric and radial velocity data. The rigorous treatment of the epoch propagation, including the effects of light-travel time, was developed by [Butkevich & Lindgren \(2014\)](#). However, for the propagation of the prior information to the *Gaia* reference epoch, it is sufficient to use the simplified treatment, which was employed in the reduction procedures used to construct the Hipparcos and Tycho catalogues, since the light-time effects are negligible

at milliarcsecond accuracy. The resultant velocity vectors of the two groups, taking Galactic rotation into account is presented in Figure 8 (right).

The treatments of proper motion velocity vectors presented in Figure 8 clearly show a marked difference in the proper motions of the two populations, in particular those of the members of L1495 and L1536. In an X-Ray survey Briceno et al. (1997) suggested that a population of stars discovered during the ROSAT mission (Trümper 1985), located to the south of the Taurus clouds, might be an older population and have a different origin from the rest of the cloud, as well as being located at a different distance to the then commonly accepted distance of 140 pc. Our initial findings tend to support these ideas and further suggest that there may be a dynamic link between L1536 and the B213 region within L1495.

Considering Figure 8 (right), one star stands out from the rest. Within the ‘far’ population, HD 30067 (Gaia DR2 147248216395196672) is found to have a markedly different velocity profile to the rest of its group. This star is noted Rebull et al. (2010) as being an A4V Class III YSO and is recorded in SIMBAD as being an A2/4 class star located at 163.5 ± 1.4 pc with a proper motion of $\mu = 16.1$ mas yr⁻¹. *Gaia* DR2 indicates a G-Band magnitude of 8.9 mag and an extinction of 4.5 mag for this source. We suggest that, although this star meets the distance and proper motion criteria described earlier, HD 30067 is actually a runaway field star and not associated with the Taurus group.

5. SUMMARY

This study has shown, through the use of trigonometric parallaxes from *Gaia* DR2, that there are significant differences in the distances to different structures within the Taurus molecular cloud complex. We have shown that there are two main associations located at 130.6 ± 0.7 and 160.2 ± 0.9 pc. The two groups have different proper motions of 24.5 ± 2.8 and 20.1 ± 2.4 mas yr⁻¹ respectively, and they appear to be moving in somewhat different directions. They also appear to have slightly different line-of-sight velocities. We call these two populations the ‘Two Horns’ of Taurus.

With this new data we have also been able to confirm that the TMR is not a coherent feature but has an extended depth of approximately 15 parsecs. We also tentatively suggest that the structure of the TMC, in general, resembles that of an inclined sheet facing away from the observer.

We thank the anonymous referees for their constructive comments. Use has been made of data from the European Space Agency (ESA) mission *GAIA* (<https://www.cosmos.esa.int/gaia>), processed by the *GAIA* Data Processing and Analysis Consortium (DPAC) (<https://www.cosmos.esa.int/web/gaia/dpac/consortium>). Funding for the DPAC has been provided by national institutions, in particular the institutions participating in the *GAIA* Multilateral Agreement.

This work has used the NASA Astrophysics Data System (ADS) Bibliographic Services (<http://ads.harvard.edu/>) as well as the VizieR catalogue access tool (<http://vizier.u-strasbg.fr/viz-bin/VizieR>) and SIMBAD astronomical database (<http://simbad.u-strasbg.fr/simbad/>), operated at CDS, Strasbourg, France.

Data products have also been used from the Two Micron All Sky Survey, which is a joint project of the University of Massachusetts and the Infrared Processing and Analysis Center/California Institute of Technology, funded by the National Aeronautics and Space Administration and the National Science Foundation.

This research has made use of *Astropy*, a community-developed core Python (<https://www.python.org/>) module for Astronomy (Robitaille et al. 2013; Price-Whelan et al. 2018). This work has also made extensive use of *Matplotlib* (Hunter 2007), *SciPy* (Van der Walt et al. 2014) and *NumPy* (Van Der Walt et al. 2011). This work would not have been possible without the countless hours put in by members of the open-source community around the world.

DWT was supported by the UK Science and Technology Facilities Council under grant number ST/R000786/1. KP acknowledges support from the Ministry of Science and Technology (Taiwan) under Grant No. 106-2119-M-007-021-MY3.

REFERENCES

- | | |
|---|---|
| Bailer-Jones, C., Rybizki, J., Fouesneau, M., Mantelet, G.,
& Andrae, R. 2018, <i>AJ</i> , 156, 58 | Bertout, C., Robichon, N., & Arenou, F. 1999, <i>A&A</i> , 352,
574 |
| Bailer-Jones, C. A. 2015, <i>PASP</i> , 127, 994 | Briceno, C., Hartmann, L. W., Stauffer, J. R., et al. 1997,
<i>AJ</i> , 113, 740 |
| Bertout, C., & Genova, F. 2006, <i>A&A</i> , 460, 499 | |

- Brown, A., Vallenari, A., Prusti, T., et al. 2018, *A&A*, 616, A1
- Butkevich, A. G., & Lindegren, L. 2014, *A&A*, 570, A62
- Clark, F. O., Giguere, P. T., & Crutcher, R. M. 1977, *ApJ*, 215, 511
- di Francesco, J., Evans, II, N. J., Caselli, P., et al. 2007, *Protostars and Planets V*, 17
- Ducourant, C., Teixeira, R., Périé, J., et al. 2005, *A&A*, 438, 769
- Dzib, S. A., Loinard, L., Rodríguez, L. F., et al. 2015, *ApJ*, 801, 91
- Elias, J. 1978, *ApJ*, 224, 857
- Esplin, T., & Luhman, K. 2017, *AJ*, 154, 134
- . 2019, *The Astronomical Journal*, 158, 54
- Feigelson, E., & Babu, G. J. 2013, *Beware the Kolmogorov-Smirnov test*, Penn State University
- Frink, S., Röser, S., Neuhäuser, R., & Sterzik, M. 1997, *A&A*, 325, 613
- Galli, P., Loinard, L., Bouy, H., et al. 2019, *Astronomy & Astrophysics*, 630, A137
- Galli, P. A., Loinard, L., Ortiz-Léon, G. N., et al. 2018, *ApJ*, 859, 33
- Goldsmith, P. F., Heyer, M., Narayanan, G., et al. 2008, *ApJ*, 680, 428
- Gomez, M., Hartmann, L., Kenyon, S., & Hewett, R. 1993, *AJ*, 105, 1927
- Gomez, M., Jones, B., Hartmann, L., et al. 1992, *AJ*, 104, 762
- Goodwin, S. P., Whitworth, A. P., & Ward-Thompson, D. 2004, *A&A*, 419, 543
- Gudel, M., Padgett, D. L., & Dougados, C. 2007, *Protostars and planets V*, 329
- Hacar, A., Tafalla, M., Kauffmann, J., & Kovács, A. 2013, *A&A*, 554, A55
- Hartigan, J. A., Hartigan, P. M., et al. 1985, *Annals of Statistics*, 13, 70
- Hartigan, P., & Kenyon, S. J. 2003, *ApJ*, 583, 334
- Hartmann, L. 2002, *ApJ*, 578, 914
- Hartmann, L., Jones, B., Stauffer, J., & Kenyon, S. 1991, *AJ*, 101, 1050
- Heiles, C., & Katz, G. 1976, *AJ*, 81, 37
- Hunter, J. D. 2007, *Computing in Science and Engineering*, 9, 90
- Jones, B., & Herbig, G. 1979, *AJ*, 84, 1872
- Kirk, J. M., Ward-Thompson, D., Palmeirim, P., et al. 2013, *MNRAS*, 432, 1424
- Kolmogorov, A. 1933, *Inst. Ital. Attuari, Giorn.*, 4, 83
- Kraus, A. L., Herczeg, G. J., Rizzuto, A. C., et al. 2017, *ApJ*, 838, 150
- Li, C., Zhao, G., & Yang, C. 2019, *ApJ*, 872, 205
- Li, D., & Goldsmith, P. F. 2012, *ApJ*, 756, 12
- Lindegren, L., & Perryman, M. 1996, *A&AS*, 116, 579
- Lindegren, L., Hernández, J., Bombrun, A., et al. 2018, *A&A*, 616, A2
- Loinard, L., Torres, R. M., Mioduszewski, A. J., et al. 2007, *The Astrophysical Journal*, 671, 546
- Luhman, K. 2018, *AJ*, 156, 271
- Luri, X., Brown, A., Sarro, L., et al. 2018, *A&A*, 616, A9
- Lynds, B. T. 1962, *ApJS*, 7, 1
- Malinen, J., Juvela, M., Rawlings, M., et al. 2012, *A&A*, 544, A50
- Marsh, K., Kirk, J., André, P., et al. 2016, *MNRAS*, 459, 342
- Maurus, S., & Plant, C. 2016, in *Proceedings of the 22nd ACM SIGKDD international conference on Knowledge discovery and data mining*, ACM, 1055–1064
- McCuskey, S. 1939, *ApJ*, 89, 568
- Meistas, E., & Straizys, V. 1981, *AcA*, 31, 85
- Mooley, K., Hillenbrand, L., Rebull, L., Padgett, D., & Knapp, G. 2013, *ApJ*, 771, 110
- Narayanan, G., Heyer, M. H., Brunt, C., et al. 2008, *ApJS*, 177, 341
- Nutter, D., Kirk, J., Stamatellos, D., & Ward-Thompson, D. 2008, *MNRAS*, 384, 755
- Oh, S., Price-Whelan, A. M., Hogg, D. W., Morton, T. D., & Spergel, D. N. 2017, *AJ*, 153, 257
- Olling, R. P., & Dehnen, W. 2003, *ApJ*, 599, 275
- Oort, J. H., et al. 1927, *Bulletin of the Astronomical Institutes of the Netherlands*, 3, 275
- Ortiz-León, G. N., Loinard, L., Dzib, S. A., et al. 2018, *ApJL*, 869, L33
- Palmeirim, P., André, P., Kirk, J., et al. 2013, *A&A*, 550, A38
- Panopoulou, G. V., Tassis, K., Goldsmith, P., & Heyer, M. 2014, *MNRAS*, 444, 2507
- Peacock, J. 1983, *MNRAS*, 202, 615
- Price-Whelan, A., Sipőcz, B., Günther, H., et al. 2018, *arXiv preprint arXiv:1801.02634*
- Rebull, L., Padgett, D., McCabe, C.-E., et al. 2010, *ApJS*, 186, 259
- Robitaille, T. P., Tollerud, E. J., Greenfield, P., et al. 2013, *A&A*, 558, A33
- Schmalzl, M., Kainulainen, J., Quanz, S. P., et al. 2010, *ApJ*, 725, 1327
- Schneider, N., Bontemps, S., Simon, R., et al. 2011, *A&A*, 529, A1
- Schönrich, R., Binney, J., & Dehnen, W. 2010, *MNRAS*, 403, 1829

- Slesnick, C. L., Carpenter, J. M., Hillenbrand, L. A., & Mamajek, E. E. 2006, *The Astronomical Journal*, 132, 2665
- Stephens, M. A. 1974, *Journal of the American statistical Association*, 69, 730
- Straizys, V., & Meistas, E. 1980, *AcA*, 30, 541
- Torres, R. M., Loinard, L., Mioduszewski, A. J., & Rodríguez, L. F. 2007, *ApJ*, 671, 1813
- . 2009, *ApJ*, 698, 242
- Tóth, L., Haas, M., Lemke, D., Mattila, K., & Onishi, T. 2004, *A&A*, 420, 533
- Trümper, J. 1985, *Bulletin d'Information du Centre de Donnees Stellaires*, 28, 81
- Van Der Walt, S., Colbert, S. C., & Varoquaux, G. 2011, *Computing in Science and Engineering*, 13, 22
- Van der Walt, S., Schönberger, J. L., Nunez-Iglesias, J., et al. 2014, *PeerJ*, 2, e453
- Walter, F., Brown, A., Linsky, J., et al. 1987, *ApJ*, 314, 297
- Zhang, Z., Liu, M. C., Best, W. M., et al. 2018, *ApJ*, 858, 41

APPENDIX

A. COMPENDIUM OF SOURCES

In this Appendix we list all of the parameters of the 168 sources in our sample, before we applied the final distance and proper motion cuts. The reader may therefore judge the validity of cutting from 168 to 161 sources.

Table 3. Properties of *Gaia* DR2 Taurus sources.

<i>Gaia</i> DR2 ID	SSTtau ID	R.A.	Dec.	Parallax	Distance	PMRA	PMDec	μ
		[deg]	[deg]	[mas]	[pc]	[mas yr ⁻¹]	[mas yr ⁻¹]	[mas yr ⁻¹]
147869573608324992	043051.7 + 24414	67.7156	24.6965	9.51	105.12	11.52	-24.50	27.10
151870352825256576	043545.2 + 273713	68.9387	27.6202	8.83	113.19	14.20	-25.79	29.44
147778490237623808	043306.6 + 240954	68.2777	24.1652	8.83	113.20	9.56	-20.23	22.37
149685627517927296	042359.7 + 251452	65.9988	25.2479	8.75	114.33	0.99	-19.70	19.72
147546080967742720	043621.5 + 235116	69.0896	23.8545	8.66	115.46	-1.54	-19.48	19.54
151296579553731456	043007.2 + 260820	67.5302	26.1390	8.62	116.06	2.67	-21.927	22.09
164513602672978304	041840.6 + 281915	64.6692	28.3209	8.52	117.44	6.62	-29.87	30.60
164513022853468160	041807.9 + 282603	64.5333	28.4342	8.48	117.95	8.43	-24.73	26.13
149409920679460096	042630.5 + 244355	66.6273	24.7321	8.41	118.91	2.74	-22.02	22.19
164502062096975744	041901.1 + 281942	64.7546	28.3282	8.38	119.37	8.71	-25.34	26.79
164598303725243776	041935.4 + 282721	64.8978	28.4560	8.36	119.64	11.93	-25.97	28.58
164550882989640192	042203.1 + 282538	65.5132	28.4274	8.31	120.27	10.27	-25.86	27.83
146874275068113664	044000.6 + 235821	70.0028	23.9724	8.30	120.49	8.62	-20.74	22.46
151262700852297728	042704.6 + 260616	66.7696	26.1044	8.25	121.18	6.16	-19.30	20.26
164546038266077824	042025.8 + 281923	65.1077	28.3232	8.19	122.13	10.66	-24.22	26.46
151102790629500288	043057.1 + 255639	67.7384	25.9442	8.14	122.82	5.42	-23.02	23.65
148116246465275520	044205.4 + 252256	70.5229	25.3822	8.14	122.88	5.49	-18.99	19.77
164507353496637952	041831.1 + 281629	64.6297	28.2747	8.12	123.08	8.82	-25.64	27.12
165563674934601856	041357.3 + 291819	63.4891	29.3053	8.10	123.47	9.95	-22.89	24.96
146764465639042176	043906.3 + 233417	69.7766	23.5716	8.06	124.14	8.18	-21.82	23.30
147799209159857280	043217.8 + 242214	68.0745	24.3707	8.05	124.17	6.26	-22.20	23.06
164519276325850752	041817.1 + 282841	64.5713	28.4782	8.04	124.37	5.79	-25.03	25.69
146675954953119104	043815.6 + 230227	69.5651	23.0409	7.98	125.24	-1.07	-17.19	17.22
164513400810646912	041842.5 + 281849	64.6771	28.3138	7.97	125.50	12.13	-24.15	27.02
164495323291866624	041851.1 + 281433	64.7132	28.2425	7.96	125.66	8.61	-24.65	26.11
164513538249595136	041847.0 + 282007	64.6960	28.3353	7.95	125.77	8.30	-25.31	26.63
164422961683000320	041941.2 + 274948	64.9220	27.8299	7.91	126.37	9.94	-24.96	26.87
152118881108855680	042445.0 + 270144	66.1878	27.0290	7.89	126.73	8.39	-26.84	28.13
146767764173923328	043858.5 + 233635	69.7442	23.6097	7.89	126.82	8.64	-21.20	22.89
163165738856771200	041514.7 + 280009	63.8114	28.0025	7.88	126.88	8.55	-25.52	26.92
146881048231272192	043933.6 + 235921	69.8902	23.9891	7.87	127.12	7.28	-20.99	22.22
152511475478780416	042155.6 + 275506	65.4819	27.9183	7.85	127.37	10.75	-27.22	29.27
151793082068521856	043114.4 + 271017	67.8102	27.1715	7.84	127.49	9.17	-27.58	29.06
164445437248152832	042026.0 + 280408	65.1087	28.0691	7.84	127.51	8.33	-26.07	27.37
146764809236423808	043901.6 + 233602	69.7568	23.6007	7.82	127.81	8.57	-21.85	23.47
162758236656524416	041447.8 + 264811	63.6995	26.8030	7.82	127.93	9.02	-22.45	24.20
148037764527442944	043619.0 + 254258	69.0796	25.7163	7.81	128.02	8.91	-27.47	28.88
163184366130809984	041412.9 + 281212	63.5539	28.2033	7.80	128.13	8.93	-29.05	30.40
147606657186323712	043527.3 + 241458	68.8641	24.2496	7.80	128.22	6.05	-20.77	21.64
151327159721125888	042945.6 + 263046	67.4403	26.5128	7.80	128.23	6.87	-20.97	22.06
147801339463632000	043301.9 + 242100	68.2582	24.3499	7.80	128.24	6.37	-20.47	21.44
162757545164429696	041447.3 + 264626	63.6971	26.7739	7.78	128.47	9.48	-22.69	24.59
163246832135164544	041314.1 + 281910	63.3090	28.3195	7.76	128.85	8.37	-24.40	25.80
164698634160139264	041733.7 + 282046	64.3906	28.3462	7.76	128.88	9.18	-25.55	27.15

Table 3 continued on next page

Table 3 (continued)

<i>Gaia</i> DR2 ID	SSTtau ID	R.A.	Dec.	Parallax	Distance	PMRA	PMDec	μ
		[deg]	[deg]	[mas]	[pc]	[mas yr ⁻¹]	[mas yr ⁻¹]	[mas yr ⁻¹]
164702070133970944	041749.6 + 282936	64.4569	28.4933	7.75	129.03	6.90	-24.62	25.57
151373820245230080	042920.7 + 263340	67.3363	26.5611	7.74	129.24	7.91	-20.41	21.89
149369139966814976	042936.0 + 243555	67.4003	24.5987	7.73	129.42	8.57	-20.20	21.94
164666022471759232	041628.1 + 280735	64.1171	28.1265	7.70	129.84	6.85	-25.90	26.80
164409359522965120	041830.3 + 274320	64.6263	27.7223	7.70	129.89	8.73	-26.27	27.68
145238687096970496	043508.5 + 231139	68.7855	23.1943	7.69	129.96	7.24	-20.98	22.19
147796013704188928	043231.7 + 242002	68.1324	24.3341	7.69	130.03	7.12	-21.50	22.65
147796013704189440	043230.5 + 241957	68.1274	24.3325	7.68	130.21	6.65	-21.86	22.85
146277553787186048	043223.2 + 240301	68.0972	24.0503	7.68	130.24	7.36	-22.43	23.60
164705368668853120	041738.9 + 283300	64.4123	28.5500	7.68	130.27	6.87	-25.25	26.17
164536250037820160	042158.8 + 281806	65.4952	28.3017	7.67	130.33	9.01	-26.39	27.88
151028990206478080	043203.2 + 252807	68.0138	25.4687	7.67	130.39	8.09	-22.81	24.20
146285112929523456	043023.6 + 235912	67.5986	23.9868	7.67	130.40	4.73	-21.97	22.48
164518589131083136	041831.1 + 282716	64.6297	28.4544	7.67	130.44	8.68	-25.10	26.56
147806733942555008	043215.4 + 242859	68.0643	24.4831	7.67	130.46	5.02	-21.38	21.96
147790202612482560	043334.0 + 242117	68.3919	24.3547	7.66	130.50	5.88	-20.55	21.38
152226491513195648	042457.0 + 271156	66.2379	27.1989	7.66	130.57	8.36	-26.75	28.02
147831571737487488	043310.0 + 243343	68.2918	24.5619	7.66	130.60	7.25	-21.23	22.43
163182888662060928	041411.8 + 281153	63.5496	28.1981	7.63	131.09	9.08	-23.89	25.56
146366442430208640	042959.5 + 243307	67.4980	24.5520	7.63	131.12	8.18	-21.44	22.95
148017561002336384	043342.9 + 252647	68.4289	25.4462	7.63	131.14	5.13	-22.77	23.35
164738521519622656	041414.5 + 282758	63.5609	28.4660	7.62	131.24	9.50	-23.57	25.41
151297958238753664	042951.5 + 260644	67.4648	26.1124	7.62	131.28	5.95	-21.01	21.84
150393571269837184	041810.7 + 251957	64.5450	25.3325	7.61	131.36	8.83	-23.34	24.95
164684340508950144	041539.1 + 281858	63.9132	28.3162	7.61	131.49	9.25	-24.38	26.08
164504467278644096	041926.2 + 282614	64.8595	28.4372	7.59	131.70	8.36	-25.47	26.81
163184366130809472	041413.5 + 281249	63.5566	28.2136	7.58	131.94	8.59	-24.42	25.88
163184091252903936	041417.0 + 281057	63.5709	28.1826	7.55	132.44	8.28	-24.16	25.54
152917298349085824	042515.5 + 282927	66.3147	28.4909	7.52	133.06	10.79	-25.05	27.27
152362491654557696	042039.1 + 271731	65.1633	27.2920	7.51	133.07	10.41	-26.09	28.09
147847072275324416	043150.5 + 242418	67.9607	24.4048	7.50	133.33	4.46	-22.96	23.39
151262876946558976	042657.3 + 260628	66.7388	26.1078	7.50	133.36	5.19	-20.71	21.35
151125919028356352	043336.7 + 260949	68.4033	26.1636	7.50	133.40	8.16	-17.37	19.19
163179521407696384	041505.1 + 280846	63.7715	28.1460	7.49	133.57	8.46	-24.48	25.90
152516079683687680	042306.0 + 280119	65.7754	28.0220	7.47	133.88	7.93	-26.68	27.84
148450085683504896	043835.2 + 261038	69.6471	26.1773	7.46	133.96	4.89	-21.78	22.32
147869784062378624	043051.3 + 244222	67.7141	24.7061	7.45	134.22	7.05	-20.94	22.10
151265002954775936	042727.9 + 261205	66.8667	26.2013	7.42	134.69	1.81	-23.45	23.52
164514053645658752	041901.9 + 282233	64.7583	28.3758	7.40	135.07	9.19	-25.76	27.35
151374198202645376	042942.4 + 263249	67.4270	26.5469	7.40	135.12	6.90	-21.21	22.30
162967384383246336	041557.9 + 274617	63.9917	27.7714	7.37	135.67	7.82	-24.65	25.86
163181342473839744	041417.6 + 28060	63.5734	28.1026	7.37	135.69	8.34	-23.32	24.76
148172179824515968	044148.2 + 253430	70.4511	25.5751	7.34	136.16	4.51	-19.61	20.12
148112913570653568	044221.0 + 252034	70.5876	25.3428	7.34	136.16	4.89	-19.42	20.03
163233981593016064	041327.2 + 281624	63.3635	28.2734	7.34	136.30	7.44	-23.84	24.97
148401565437820928	044008.0 + 260525	70.0334	26.0903	7.34	136.32	5.73	-20.13	20.93
148400229703257856	043944.8 + 260152	69.9370	26.0312	7.31	136.85	7.46	-22.11	23.33
153001307909276928	042916.2 + 285627	67.3176	28.9409	7.30	137.05	-6.78	5.99	9.05
147818450613367424	043455.4 + 242853	68.7309	24.4813	7.29	137.20	3.48	-20.99	21.27
164470794735041152	041618.8 + 275215	64.0786	27.8708	7.28	137.29	7.47	-24.93	26.02
164506116546058112	041749.5 + 281331	64.4565	28.2254	7.28	137.37	8.81	-25.22	26.71
164474986623118592	041612.1 + 275638	64.0505	27.9439	7.27	137.49	8.89	-25.72	27.21
152029992465874560	042420.9 + 263051	66.0871	26.5141	7.27	137.59	9.25	-27.37	28.89

Table 3 continued on next page

Table 3 (continued)

<i>Gaia</i> DR2 ID	SSTtau ID	R.A.	Dec.	Parallax	Distance	PMRA	PMDec	μ
		[deg]	[deg]	[mas]	[pc]	[mas yr ⁻¹]	[mas yr ⁻¹]	[mas yr ⁻¹]
148449845165337600	043821.3 + 260913	69.5889	26.1537	7.23	138.31	5.47	-22.97	23.62
152518828462749440	042307.7 + 280557	65.7824	28.0992	7.19	139.05	9.65	-27.01	28.69
148449913884294528	043828.5 + 261049	69.6191	26.1803	7.17	139.38	6.13	-21.34	22.20
151262941369626752	042654.4 + 260651	66.7267	26.1141	7.15	139.91	3.98	-20.40	20.79
145157937416226176	043559.4 + 223829	68.9980	22.6413	7.13	140.33	11.85	-16.94	20.67
148384179410294272	044108.2 + 255607	70.2845	25.9353	7.10	140.83	7.20	-21.95	23.10
147441558642852736	044427.1 + 251216	71.1131	25.2045	7.09	141.01	6.45	-20.15	21.16
147679014500233728	044018.8 + 243234	70.0786	24.5427	7.07	141.50	-1.41	-43.35	43.38
163181308112262400	041426.2 + 280603	63.6095	28.1008	7.04	142.13	5.54	-27.64	28.19
151787064819255936	043126.6 + 270318	67.8613	27.0551	6.99	143.08	13.99	-19.89	24.32
148354733113981696	043903.9 + 254426	69.7665	25.7406	6.95	143.99	7.04	-20.61	21.77
148106316500918272	044303.0 + 252018	70.7628	25.3384	6.92	144.57	4.73	-20.21	20.75
163229544890946944	041353.2 + 281123	63.4721	28.1897	6.91	144.80	11.32	-22.68	25.35
148450875956969344	043814.8 + 261139	69.5620	26.1943	6.88	145.41	4.01	-23.17	23.51
148420639387738112	043800.8 + 255857	69.5036	25.9825	6.87	145.50	4.90	-22.63	23.16
152643240779301632	042900.6 + 275503	67.2529	27.9175	6.87	145.65	8.65	-25.26	26.70
145196527698016512	043319.0 + 224634	68.3295	22.7761	6.77	147.67	10.94	-20.15	22.93
145947077527182848	043309.4 + 224648	68.2895	22.7801	6.71	148.98	10.67	-16.76	19.87
148374391180009600	043955.7 + 254502	69.9823	25.7505	6.70	149.27	6.19	-20.34	21.26
150501362066641664	042216.4 + 254911	65.5686	25.8199	6.61	151.26	14.13	-19.65	24.20
148141775750936960	044039.7 + 251906	70.1658	25.3183	6.57	152.20	6.35	-20.57	21.53
151130591952773632	043307.8 + 261606	68.2826	26.2684	6.57	152.25	7.17	-17.31	18.74
151037064744973696	043158.4 + 254329	67.9936	25.7249	6.55	152.60	7.55	-21.14	22.45
145133786815830784	043541.8 + 223411	68.9244	22.5698	6.53	153.25	10.96	-17.96	21.04
147373010964871040	044642.6 + 245903	71.6776	24.9842	6.48	154.25	4.60	-19.52	20.06
152109054223716480	042423.2 + 265008	66.0968	26.8356	6.46	154.73	11.49	-18.35	21.65
145950895754320384	043224.1 + 225108	68.1007	22.8522	6.44	155.36	9.99	-17.43	20.09
152108882425024128	042426.4 + 264950	66.1103	26.8305	6.43	155.51	11.58	-17.86	21.29
151283870746458496	042629.3 + 262413	66.6225	26.4037	6.42	155.88	10.90	-17.85	20.92
145209442664192896	043552.8 + 225058	68.9703	22.8495	6.39	156.53	10.95	-16.53	19.83
148196510814073728	044110.7 + 255511	70.2950	25.9198	6.38	156.81	4.52	-20.11	20.61
163183644576299264	041449.2 + 281230	63.7054	28.2084	6.37	156.92	10.65	-21.17	23.70
145213192171160064	043553.4 + 225408	68.9730	22.9024	6.36	157.15	11.37	-18.48	21.70
152288824375681536	042216.7 + 265457	65.5699	26.9158	6.35	157.57	11.31	-17.60	20.92
152098299625634816	042247.8 + 264553	65.6996	26.7646	6.34	157.67	10.74	-17.14	20.23
145209618758377856	043547.3 + 225021	68.9473	22.8393	6.30	158.63	13.52	-15.90	20.87
145203159127518336	043352.0 + 225030	68.4668	22.8416	6.30	158.71	8.90	-17.07	19.25
144936836795636864	043917.7 + 222103	69.8242	22.3509	6.29	158.87	10.47	-17.38	20.29
145157941711889536	043558.9 + 223835	68.9956	22.6431	6.29	158.94	10.81	-15.77	19.12
145196252820109440	043326.2 + 224529	68.3593	22.7581	6.28	159.17	8.62	-16.75	18.84
145213295250374016	043552.0 + 225503	68.9671	22.9177	6.28	159.22	8.78	-8.09	11.94
148010281032823552	043339.0 + 252038	68.4129	25.3438	6.28	159.34	9.33	-18.29	20.53
152000786688289664	042444.5 + 261014	66.1858	26.1705	6.27	159.57	11.87	-17.32	21.00
148289831863907840	044138.8 + 255626	70.4118	25.9407	6.26	159.78	2.50	-15.48	15.68
164800235906366976	041542.7 + 290959	63.9283	29.1665	6.25	159.95	12.34	-17.75	21.62
164783811951433856	041639.1 + 285849	64.1631	28.9803	6.25	160.04	4.97	-15.00	15.80
148116276529733120	044207.7 + 252311	70.5325	25.3866	6.25	160.12	-0.74	-14.15	14.17
146319193494413696	042745.3 + 235724	66.9392	23.9567	6.24	160.18	11.27	-16.57	20.04
152293149405058816	042146.3 + 265929	65.4430	26.9914	6.23	160.47	11.92	-18.33	21.86
152104381299305600	042449.0 + 264310	66.2044	26.7195	6.21	160.97	10.61	-17.05	20.08
145132927822383616	043520.2 + 223214	68.8343	22.5373	6.20	161.40	9.83	-16.63	19.32
145203811962545152	043410.9 + 225144	68.5459	22.8623	6.18	161.77	8.90	-17.27	19.43
145213875069914496	043520.8 + 225424	68.8371	22.9066	6.18	161.83	9.72	-19.25	21.56

Table 3 continued on next page

Table 3 (*continued*)

<i>Gaia</i> DR2 ID	SSTtau ID	R.A.	Dec.	Parallax	Distance	PMRA	PMDec	μ
		[deg]	[deg]	[mas]	[pc]	[mas yr ⁻¹]	[mas yr ⁻¹]	[mas yr ⁻¹]
145212711134828672	043542.0 + 225222	68.9252	22.8729	6.17	162.07	10.02	-16.77	19.54
145210099794710272	043551.0 + 225240	68.9629	22.8777	6.16	162.32	6.32	-28.15	28.85
145225596036660224	043456.9 + 225835	68.7373	22.9765	6.15	162.68	11.70	-16.41	20.16
147562470562750720	043649.1 + 241258	69.2049	24.2163	6.14	162.85	43.42	-13.26	45.40
152099055539792000	042224.0 + 264625	65.6002	26.7738	6.13	163.27	11.41	-17.86	21.19
147248216395196672	044518.2 + 242436	71.3258	24.4101	6.11	163.54	-15.85	-2.85	16.10
145951789107603200	043249.1 + 225302	68.2047	22.8841	6.08	164.53	7.43	-15.79	17.45
145213192171159552	043554.1 + 225413	68.9757	22.9037	6.03	165.95	11.87	-9.99	15.51
152305248330621184	042134.5 + 270138	65.3942	27.0273	5.99	167.00	11.77	-16.63	20.38
164800815725933312	041524.0 + 291043	63.8505	29.1787	5.97	167.54	10.74	-19.44	22.20
152349022637314176	042025.5 + 270035	65.1065	27.0098	5.87	170.35	11.35	-17.73	21.05
145220064117853696	043610.3 + 225956	69.0433	22.9988	5.84	171.24	10.81	-15.96	19.27
146050057959093632	043119.0 + 233504	67.8295	23.5846	5.83	171.56	8.08	-16.60	18.47
145203704587705088	043415.2 + 225030	68.5637	22.8418	5.82	171.97	10.08	-17.50	20.19
151129011404806912	043344.6 + 261500	68.4361	26.2500	5.77	173.26	6.51	-17.31	18.50
145213187879627776	043552.7 + 225423	68.9700	22.9064	5.64	177.15	8.82	-13.95	16.51
145217379763796992	043638.9 + 225811	69.1622	22.9699	5.44	183.91	9.55	-15.97	18.61
152361426502650496	042115.2 + 272101	65.3136	27.3502	5.41	184.86	2.96	-4.53	5.41